



# Diagnosis and prognosis of battery degradation through re-evaluation and Gaussian process regression of electrochemical model parameters

Moritz Streb<sup>a,\*</sup>, Mathilda Ohrelius<sup>a</sup>, Aamer Siddiqui<sup>b,c</sup>, Matilda Klett<sup>b</sup>, Göran Lindbergh<sup>a</sup>

<sup>a</sup> Applied Electrochemistry, Department of Chemical Engineering, School of Engineering Sciences in Chemistry, Biotechnology and Health, KTH Royal Institute of Technology, SE-100 44, Stockholm, Sweden

<sup>b</sup> Scania CV AB, Granparksvägen 10, 151 48, Södertälje, Sweden

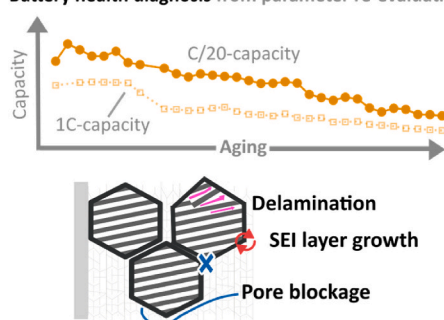
<sup>c</sup> Structural Chemistry, Department of Chemistry - Ångström Laboratory, Uppsala University, Lägerhyddsvägen 1, 751 21, Uppsala, Sweden

## HIGHLIGHTS

- Tracking electrochemical model parameters using novel reference performance test.
- Diagnosis of degradation based on changes of electrochemical parameters.
- Gaussian process regression extrapolation of electrochemical parameter trajectories.
- Prognosis of battery state-of-health using extrapolated electrochemical model.

## GRAPHICAL ABSTRACT

### Battery health diagnosis from parameter re-evaluation



### Lifetime prognosis via Gaussian process regression of electrochemical parameters



## ARTICLE INFO

### Keywords:

Lithium-ion battery modelling  
State-of-health diagnosis  
Electrochemical model  
Gaussian process regression  
Lifetime prognosis

## ABSTRACT

Lithium-ion battery degradation is complex, and many mechanisms occur concurrently. In-depth degradation is traditionally investigated by post-mortem characterization in lab-settings. If mechanisms could instead be identified in-operando, utilization could be adjusted, and battery lifetime extended. We investigate changes in electrochemical model parameters during battery testing and their correlation with degradation observed in a traditional post-mortem characterization. Commercial batteries are cycle-aged using different stationary storage service cycles and a novel reference performance test is applied intermittently. This test is based on current profiles optimally designed with respect to maximized sensitivity for individual electrochemical parameters and embedded within a charging procedure. Usage dependency of parameter trajectories over the course of ageing is demonstrated and coupled to observed micro-structural changes. Subsequently, the parameter trajectories are extrapolated using Gaussian Process Regression for physics-based state-of-health estimation and remaining-useful-life prediction. We demonstrate and validate estimation of full cell performance under constant load at a later state in life.

\* Corresponding author.

E-mail address: [streb@kth.se](mailto:streb@kth.se) (M. Streb).

<https://doi.org/10.1016/j.jpowsour.2023.233686>

Received 3 July 2023; Received in revised form 22 September 2023; Accepted 28 September 2023

Available online 19 October 2023

0378-7753/© 2023 The Authors. Published by Elsevier B.V. This is an open access article under the CC BY license (<http://creativecommons.org/licenses/by/4.0/>).

## 1. Introduction

Electrification of personal and commercial vehicles is strongly tied to the success of the lithium-ion battery technology [1]. While adoption is widespread, many issues remain. This includes fast charging [2], cycle life [3] as well as raw material supply [4] and recycling [5]. Increasing the lifespan of lithium-ion batteries decreases both the tension in raw material supply and dampens required recycling needs. This can be achieved in two ways, firstly, by improved cell and system design and material development, or secondly by more efficient and smart usage. The latter includes second life [6] or vehicle-to-grid applications [7] but also aging-sensitive battery control while the system is in use.

Control of batteries in the battery management system (BMS) is responsible for safe operation and maximizing battery lifetime [8] and traditionally uses empirical models based on laboratory characterization and expert knowledge [9]. Advanced BMS using electrochemical models have successfully been demonstrated for adaptive fast-charging [10] or state-of-health (SOH) estimation [11]. These models are based on a physical description of the internal processes of the battery and contain a large number of parameters that must be determined either experimentally or by parameter estimation from input-output data [9]. Many aging phenomena are known to impact battery capacity and rate-capability [3]. These phenomena can stem from unwanted side-reactions and be manifested for instance as a solid-electrolyte-interphase (SEI) that causes a resistive surface layer. An accurate physical description of such a system over time therefore requires either discrete aging models that directly predict the increasing layer thickness based on driving pattern, or a surface-layer resistance parameter that must be updated intermittently [8]. The latter approach is more flexible in general, as it does not make a-priori assumptions about which aging will be observed and is also applicable for cells with unknown histories. Sulzer et al. [12] suggest that advanced reference performance tests (RPTs) could be used to estimate parameters of physics-based models beyond resistance and capacity. In this work, we demonstrate a novel re-parametrization strategy for 7 dynamic and 3 balancing parameters of the full-order Doyle-Fuller-Newman model [13] throughout the cycle life of 12 commercial Ni-rich batteries.

Bi et al. [11] implemented a particle filter to correct predicted parameters of a reduced-order model in online settings for 220 cycles. Mayilvahanan et al. [14,15] first developed a machine learning based parametrization scheme for a physics-based model and then evaluated model parameters for a lithium-trivanadate electrode during 100 cycles. They then perform degradation analysis based solely on the parameter estimates and propose links to aging mechanisms. Lyu et al. [16] estimate dynamic parameters for a single particle model on a current pulse-train and observed significant changes during 140 cycles. Assumptions made in the reduced-order models might lack important features, such as electrolyte dynamics, necessary to track the internal degradation. Further, no experimental characterization has been reported to support the presented analyses.

Beyond the diagnosis of present battery health lies the prognosis of battery lifetime. Gaussian process regression has received significant attention from researchers [17–19] for forecasting battery lifetime. Richardson et al. [17] highlighted the intricacies of kernel design and proposed the usage of multiple correlated observations to predict the capacity decay based only on capacity observations. Yang et al. [18] extracted features of a charging procedure as indicators for the state-of-health and showed that a Gaussian process trained on such informative features could accurately predict battery discharge capacity. Tagade et al. [19] used the complete available voltage, current and temperature signals as input to train a deep gaussian process and showed how electrochemical parameters correlated with hidden layer output of the deep gaussian process. To the authors' knowledge, no previous work investigated Gaussian processes to learn and predict electrochemical model parameter trajectories directly.

In previous work, we developed and demonstrated a methodology

for global optimal experiment design [20]. One optimal experiment was designed per target parameter for which Sobol sensitivity is maximized. This ensures that both impact of the target is maximized, and impact of other parameters is muted. The short optimal experiments (OEs) were then included in a charging procedure making it suitable for overnight charging in vehicle applications. This intermittent RPT was then experimentally performed during a degradation study presented in Ref. [21] where batteries were cycle-aged using several stationary storage service cycles. In the present study the model parameters are estimated for every cell at every checkpoint.

We summarize the key contributions of this work as follows.

1. Demonstration of optimal experiment design RPT for commercial Ni-rich lithium-ion batteries during a cycling study with up to 2200 equivalent full cycles. We show for the first time that it is possible to track model parameters of the full-order Doyle-Fuller-Newman (DFN) model using a full-cell RPT. The changes in parameter values over time depend significantly on cell usage in 3 cycle- and 3 calendar-aging protocols.
2. Thorough validation of parameter identifiability and model performance through identifiability analysis and cross validation. This shows that the designed RPTs made all model parameters identifiable and cross validation confirmed that updating both balancing and dynamic model parameters is critical for accurate state prediction required for electrochemical control applications.
3. Correlation of observed parameter changes with post-mortem characterization. This highlights how estimated model parameters are a useful diagnostic tool for aging.
4. Extrapolation of estimated electrochemical parameter trajectories using Gaussian Process Regression (GPR). We demonstrate this fusion of machine learning and physics-based model for the first time. GPR is used to extrapolate parameter values and predict dynamic battery behavior.

The paper's contributions are summarized in Fig. 1 and the work is organized as follows: first, the physics-based model is summarized, and the targeted model parameters are introduced. We then briefly summarize the previously developed optimal experiment design methodology and show the identified experiments. Next, GPR is introduced, and the experimental procedure and set-ups are described. We begin the results section by showing the capacity fade of the investigated cells. Then, the estimated parameters are presented and discussed. This is followed by the trajectory extrapolation and a thorough validation of model performance, parameter identifiability, trajectory extrapolation accuracy, and a correlation of post-mortem characterization with the observed parameter estimates.

## 2. Physics-based model

### 2.1. Model parameters and governing equations

The Doyle-Fuller-Newman model equations and required parameters are given in Table 1 and Table 2. As this model is a standard formulation and commonly cited we leave a thorough discussion to existing literature, e.g., Refs. [13,22]. The balancing model that determines the relationship between half-cell state-of-lithiation and full-cell state-of-charge is briefly summarized. This work utilizes the PybaMM implementation [23] of the DFN model.

Firstly, measured half-cell potentials  $U_{\pm} = f(\text{SOL}_{\pm})$  prescribe a relationship between open-circuit potential (OCP) and state-of-lithiation (SOL). With given maximum concentrations  $c_{\text{max},\pm}$  the half-cell hosting capacity can be evaluated from the volume of the porous domains  $v_{\pm} = 2\epsilon_{a,\pm} w_{el} h_{el}$ :

$$q_{\pm,host} = c_{\text{max},\pm} v_{\pm} F$$

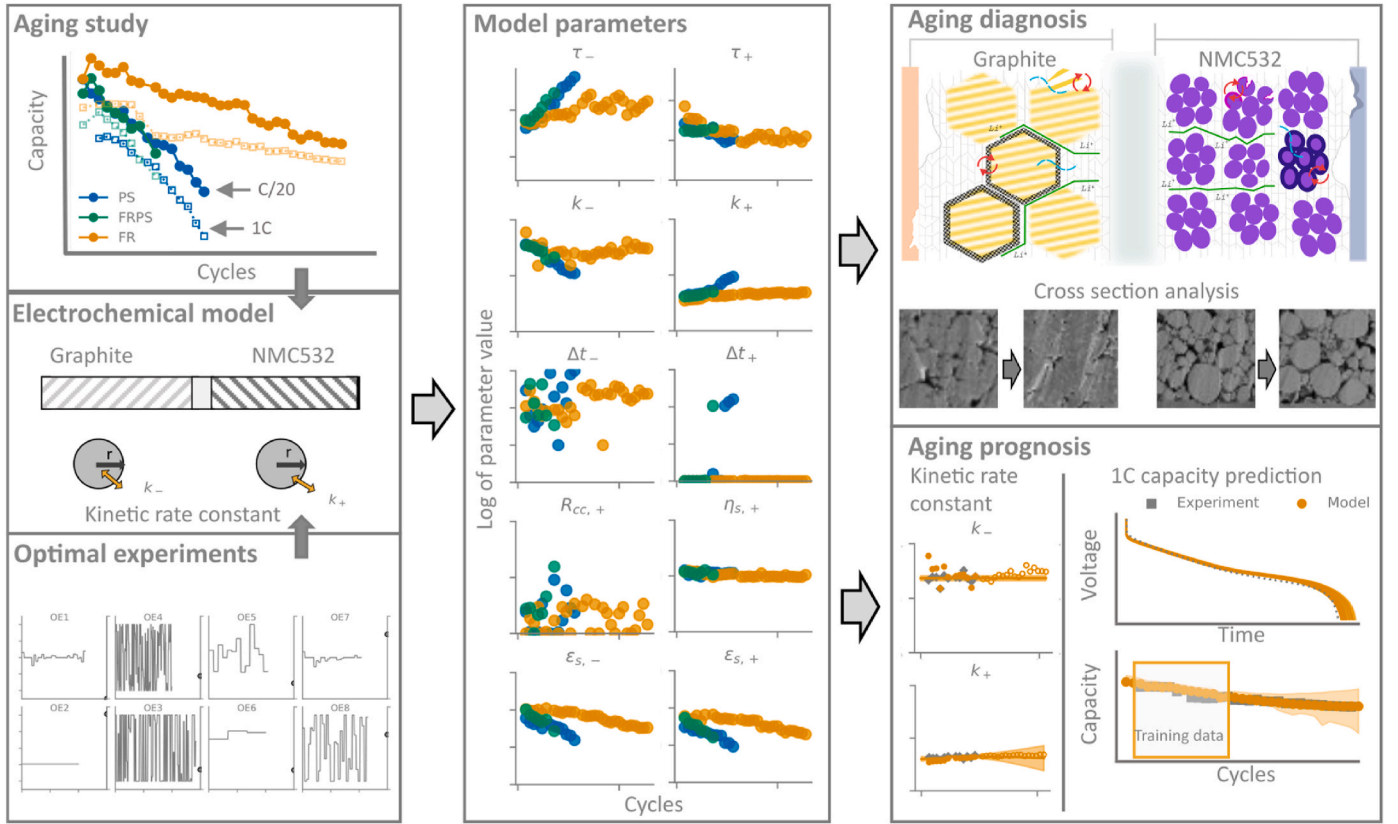


**Fig. 1.** Paper outline. Optimal experiments are performed as part of a novel reference performance test during an aging study on commercial Ni-rich lithium-ion batteries. The electrochemical model is used to estimate 10 model parameters during the lifetime of the batteries. The parameters are then used to diagnose the microscopic state-of-health of the individual cells. Parameter trends are extrapolated using gaussian process regression and the predicted parameterized model is validated against measured 1C discharge capacities.

The total available capacity must be distributed between the positive and negative half-cell:

$$q_{Li} = SOL_+ q_{+,host} + SOL_- q_{-,host} \quad 2$$

This yields:

$$SOL_- = (\eta_{s,+} - SOL_+) \frac{q_{+,host}}{q_{-,host}} \quad 3$$

Where we define  $\eta_{s,+} = q_{Li}/q_{+,host}$  as the ratio between cyclable lithium and available hosting capacity in the positive electrode.

The model given in Table 2 is then fitted to a slow-rate constant current experiment between 100 and 0% state-of-charge (SOC) to estimate three balancing parameters  $\epsilon_{a,+}$ ,  $\epsilon_{a,-}$ , and  $\eta_{s,+}$ . This then allows evaluation of the initial concentrations  $c_{init,\pm}$  in both electrodes. Note that determining the active volume fraction in this way will result in a changed estimate for the electrode surface area according to Eq. 8 and we do take this into account in our discussion of parameter changes in section 5.

## 2.2. Investigated parameters

In previous work [20] we targeted 8 model parameters with 8 parameter specific optimal experiments (OEs). We investigated the diffusion coefficient in the negative and positive electrode, the particle diameter in the positive electrode, the Bruggeman coefficient in the positive electrode, reaction rate-constants in both electrodes ( $k_{\pm}$ ), the negative electrode porosity, and the solid electrolyte interphase (SEI) layer thickness. Due to low sensitivity, the SEI layer thickness parameter was discarded. In more recent work [8] we found that the negative electrode porosity is most important for the estimation of the electrolyte

tortuosity for adjusting electrolyte transport properties and does not significantly impact electrolyte accumulation in Eq. 4. We therefore directly fit electrolyte tortuosities  $\tau_{\pm}$ . In both electrodes instead of the Bruggeman coefficient in the positive electrode and the porosity in the negative electrode in this work. Furthermore, we lumped electrode radii and diffusion coefficients into diffusion time constants  $\Delta t_{\pm}$ . This yields a set of two parameters for solid diffusion in the active material, two parameters for reaction kinetics, and two parameters for electrolyte transport. Additionally, we add a lumped resistance parameter  $R_{cc,+}$  that is neither distributed in the porous electrode nor has SOL dependency. The parameters studied estimation ranges, and identification experiments are summarized in Table 3. Parameter constraints are used to aid the parameter estimation procedure by limiting the search space to physically meaningful values. With a known parametrization for this cell-type from previous work [20], ranges were adjusted to reduce computational cost during the optimization procedure.

Note that the used reaction rate constants  $k$  include the electrolyte concentration [28]  $k_{\pm} = \hat{k}_{\pm} F / \sqrt{c_{e,0}}$ .

## 3. Methodology

### 3.1. Global optimal experiment design

In previous work [20], we developed a methodology to derive optimal experiments for parameter estimation in the DFN model. We shortly summarize the methodology here, interested readers are referred to the original work [20]. The eight optimal experiments are reproduced in Figure S1.

Candidate experiments were algorithmically generated based on three experiment design variables defining initial SOC, current

**Table 1**

DFN model parameters, the  $\pm$  index indicates parameters have distinct values in positive and negative electrode. Measured parameters are denoted with m, fitted parameters with f, and assumed parameters with a.

Symbol	Description	Source		
Dependent variables				
$\varphi_{\pm}$	Potential in the solid phase			
$\varphi_e$	Potential in the electrolyte phase			
$c_e$	Concentration in the electrolyte			
$c_{\pm}$	Concentration in the active material			
Particle Domain	Positive electrode	Negative electrode		
$\Delta t_{\pm} = \frac{r_{\pm}^2}{D_{\pm}}$	Active material diffusion time constant	f	f	
$d_{\pm} = 2r_{\pm}$	Active material particle diameter	$10 \times 10^{-6}$ m	$15 \times 10^{-6}$ m	m, m
Electrode Domain	Positive electrode	Negative electrode		
Porous electrode properties				
$\sigma_{\pm}$	Solid phase conductivity	100 S.m-1	100 S.m-1	[24, 24]
$Br_{s,\pm}$	Solid phase Bruggeman coefficient	1.5	1.5	a, a
$\tau_{\pm}$	Electrolyte tortuosity	f	f	
$k_{\pm}$	Charge-transfer reaction rate constant	f	f	
$\alpha_{a,\pm}, \alpha_{c,\pm}$	Anodic, cathodic charge-transfer coefficient	0.5/0.5	0.5/0.5	a, a
$U_{\pm}$	Open circuit potential	f ( $c_e$ )	f ( $c_e$ )	m, m
$\varepsilon_{\pm}$	Electrode porosity	0.35	0.34	a, a
$\varepsilon_{s,\pm}$	Electrode active material volume fraction	f	f	
$L_{\pm}$	Electrode thickness	$7.35 \times 10^{-5}$ m	$6.2 \times 10^{-5}$ m	m, m
$c_{max,\pm}$	Max. concentration in active material	48,240 mol.m-3	28,746 mol.m-3	a [25],
$c_{init,\pm}$	Initial concentration in active material	f ( $SOL_{+}$ )	f ( $SOL_{-}$ )	
$w_{sei}$	SEI layer thickness		$5 \times 10^{-9}$ m	- [26],
$\kappa_{sei}$	SEI layer conductivity		$5 \times 10^{-6}$ S.m-1	- [26],
$h_{el}$	Electrode height	0.645 m	0.645 m	m, m
$w_{el}$	Electrode width	0.059 m	0.059 m	m, m
Electrolyte properties				
$D_e$	Electrolyte diffusion coefficient	f ( $c_e$ )		[27]
$\kappa$	Electrolyte conductivity	f ( $c_e$ )		[27]
$t_0^{+}$	Electrolyte cationic transference number	f ( $c_e$ )		[27]
$1 + \frac{\partial f_{\pm}}{\partial \ln c_e}$	Activity coefficient	f ( $c_e$ )		[27]
$c_{e,0}$	Initial salt concentration in electrolyte	1000 mol.m-3		[27]
Separator properties				
$\varepsilon_{sep}$	Separator porosity	0.4		[25]
$Br_{sep}$	Separator Bruggeman coefficient	1.5		[25]
$L_{sep}$	Separator thickness	$1.2 \times 10^{-5}$ m		[25]

magnitude, and experiment dynamics. A candidate was then investigated by means of a global sensitivity analysis. Sobol' sensitivity indices quantify all investigated model parameters' contribution to model variance. High contribution is detrimental to model parameter identifiability. This was formalized by a single objective criterion that maximizes the Sobol' index of the target model parameter. A Bayesian

**Table 2**

DFN model equations, boundary, and initial conditions.

Equation	Boundary condition	Eq. no.
<b>Li + transport in electrolyte phase</b>		
$\frac{\partial c_e}{\partial t} + \nabla \cdot (-D_e^{eff} \nabla c_e) = \left(\frac{1-t_0^{+}}{F}\right) i_{tot}$	$\frac{\partial c_e}{\partial x} \Big _{x=0,L} = 0$	4, 5
$D_e^{eff}(c_e) = D_e(c_e) \frac{\varepsilon_{\pm}}{\tau_{\pm}}$		6
$i_{tot} = i_{loc,\pm} a_{\pm}$		7
$a_{\pm} = \frac{3\varepsilon_{s,\pm}}{r_{\pm}}$		8
<b>Charge conservation</b>		
<b>Electrode domain</b>		
$\nabla \cdot (-\sigma_{\pm}^{eff} \nabla \Phi_{\pm}) = -i_{tot}$	$\Phi_{-} _{x=0} = 0$	9, 10
	$\sigma_{-}^{eff} \frac{\partial \Phi_{-}}{\partial x} \Big _{x=L_{-}} = 0$	11
	$\sigma_{+}^{eff} \frac{\partial \Phi_{+}}{\partial x} \Big _{x=L_{-}+L_{+}} = 0$	12
	$\sigma_{+}^{eff} \frac{\partial \Phi_{+}}{\partial x} \Big _{x=L} = -\frac{I_{cell}}{A_{cell}}$	13
$\sigma_{\pm}^{eff} = \sigma_{\pm} \frac{\varepsilon_{s,\pm}}{\tau_{s,\pm}}$		14
<b>Electrolyte domain</b>		
$\nabla \cdot (-\kappa_{\pm}^{eff} \nabla \Phi_e) + \nabla \cdot (\kappa_{D,\pm}^{eff} \nabla \ln c_e) = i_{tot}$	$\frac{\partial \Phi_e}{\partial x} \Big _{x=0,L} = 0$	15, 16
	$\frac{\partial c_e}{\partial x} \Big _{x=0,L} = 0$	17
$\kappa_{\pm}^{eff}(c_e) = \kappa(c_e) \frac{\varepsilon_{\pm}}{\tau_{\pm}}$		18
$\kappa_{D,\pm}^{eff} = \frac{2RT\kappa_{\pm}^{eff}}{F} \left(1 + \frac{\partial \ln f_{\pm}}{\partial \ln c_e}\right) (1 - t_0^{+})$		19
<b>Charge transfer kinetics</b>		
$i_{loc,\pm} = i_{0,\pm} \left[ \exp\left(\frac{\alpha_{a,\pm} F}{RT} \eta_{\pm}\right) - \exp\left(-\frac{\alpha_{c,\pm} F}{RT} \eta_{\pm}\right) \right]$		20
$i_{0,\pm} =$		21
$F\hat{k}_{\pm}(c_{max,\pm} - c_{surf,\pm})^{\alpha_{a,\pm}} (c_{surf,\pm})^{\alpha_{c,\pm}} \left(\frac{c_e}{c_{e,0}}\right)^{\alpha_{e,\pm}}$		
$\eta_{\pm} = \Phi_{\pm} - \Phi_e - U_{\pm} - i_{loc,\pm} R_{film,\pm}$		22
$R_{film,\pm} = \frac{w_{SEI}}{\kappa_{SEI}} R_{film,+} = 0$		23
<b>Lithium transport in particle domain</b>		
$\frac{\partial c_{\pm}}{\partial t} = \frac{1}{r_{\pm}^2} \frac{\partial}{\partial r} \left( D_{\pm} r_{\pm}^2 \frac{\partial c_{\pm}}{\partial r} \right)$	$\frac{\partial c_{\pm}}{\partial r} \Big _{r=0} = 0$	24, 25
	$D_{\pm} \frac{\partial c_{\pm}}{\partial r} \Big _{r=R_{\pm}} = -\frac{i_{loc,\pm}}{F}$	26
$t_{\pm} = r_{\pm}^2 / D_{\pm}$		27
<b>Porous media properties</b>		
$\tau_{s,\pm} = \varepsilon_{s,\pm}^{1-Br_{s,\pm}}$		28
<b>Cell voltage</b>		
$U_{cell} = \Phi_{+} _{x=L_{-}+L_{+}} - \Phi_{-} _{x=0} - I_{cell} R_{cc,+}$		29

optimization algorithm determined one optimal experiment per target parameter by exploring the space of possible experiments.

The methodology's benefits were demonstrated in a thorough experimental validation. We investigated a commercial 2.6 Ah cylindrical cell with a LiNi<sub>0.5</sub>Mn<sub>0.3</sub>Co<sub>0.2</sub>O<sub>2</sub> (NMC532) positive and a graphite negative electrode. Our validation showed that physics-based models parametrized with OEs had 40% reduced root-mean-square error (RMSE). We further constructed three-electrode cells from harvested electrode samples and confirmed the improved model performance in half-cell validation [20].

### 3.2. Parameter estimation

Model parameters are estimated by minimizing the residual difference between model predicted cell voltage  $y(\hat{\theta})$  with parameter estimates  $\hat{\theta}$  and the measured cell voltage  $y_m$ . We use a least-squares estimator, this is theoretical equivalent to maximum likelihood estimation for gaussian residuals [9]. This is a classical non-linear least-squares problem and many algorithms for its solution exist. This procedure will yield a parameter-set that fits a given measurement best



**Table 3**

Investigated model parameters, feasible identification ranges and the experiment they are determined from.

Symbol	Name	Feasible Range	Experiment
$\Delta t_-$	Negative electrode diffusion time constant	[100, 10,000]	OE1-OE8
$\Delta t_+$	Positive electrode diffusion time constant	[1, 2000]	OE2-OE8
$k_-$	Negative reaction rate constant	$[1 \times 10^{-7}, 1 \times 10^{-2}]$	OE2-OE8
$k_+$	Positive reaction rate constant	$[1 \times 10^{-7}, 1 \times 10^{-3}]$	OE2-OE8
$\tau_-$	Negative electrolyte tortuosity	[4, 15]	OE2-OE8
$\tau_+$	Positive electrolyte tortuosity	[0.5, 6]	OE2-OE8
$R_{cc,+}$	Positive current collector bulk resistance	$[1 \times 10^{-4}, 1 \times 10^{-1}]$	OE2-OE8
$\varepsilon_{s,-}$	Negative electrode active material volume fraction	[0.5, 0.75]	C/20 discharge
$\varepsilon_{s,+}$	Positive electrode active material volume fraction	[0.5, 0.75]	C/20 discharge
$\eta_{s,+}$	Positive electrode utilization	[0.95, 1.02]	C/20 discharge

and is therefore inherently bound by model limitations. We cannot show the estimated parameters are *true*, only that they are identifiable (via identifiability analysis), predictive (via cross validation) and consistent with post-mortem characteristics.

We employ the gradient free algorithm developed by Cartis et al. [29]. The upper and lower bounds  $\theta_u$  and  $\theta_l$  are chosen to include physically feasible parameter values. Note that bounds are merely guiding the optimizer where to search and thereby reducing computational cost. A global algorithm with infinite resources will converge to the same global optimum for any initial value set. We perform a two-step estimation where the first step estimates three balancing parameters using C/20 discharge curves and the second step estimates dynamic model parameters from the optimal experiments. During the balancing step (step 1), dynamic model parameters are kept fixed at their nominal values. The impact of unknown dynamic parameters is assumed to be negligible at the used C/20 rate.

We previously proposed a multi-step procedure for identification of dynamic parameters in step 2 [20] but had to slightly deviate in this work as increase in polarization caused OE1 to be started before equilibrium was reached. To avoid this systematic error influencing estimation on all model parameters this experiment is only included in the estimation of parameter  $\Delta t_-$ . As this experiment (OE1) is modeled as starting from an initial equilibrium but during later checkups the experiment was started before equilibrium is reached, this will likely cause a higher uncertainty in the  $\Delta t_-$  estimate. The updated procedure for dynamic parameters (step 2) therefore first estimates all dynamic parameters except  $\Delta t_-$  on all experiments except OE1. These estimates are fixed and then  $\Delta t_-$  is estimated on all OEs (see Table 3).

$$\text{minimize } \sum_{k=0}^N (y(k, \hat{\theta}) - y_m(k))^2 \quad 30$$

$$\text{subject to } \theta_l \leq \hat{\theta} \leq \theta_u \quad 31$$

### 3.3. Gaussian process regression

Gaussian process regression (GPR) is used to extrapolate from estimated parameter estimates. GPR is a form of non-parametric regression. The summary below is based on the more elaborate discussion in Ref. [30] and the implementation in the present work is based on [31]. The prior of regression function is a Gaussian Process (GP):

$$f(x) \sim GP(m(x), \kappa(x, x')) \quad 32$$

Where the mean function is set to zero in this case:

$$m(x) = 0 \quad 33$$

and the kernel function

$$\kappa(x, x') = E[(f(x) - m(x))(f(x') - m(x'))^T] \quad 34$$

For any finite set of inputs  $X = x_1, \dots, x_N$  this defines a gaussian distribution with the mean ( $m(X) = 0$  In this case) and the covariance function  $K(X)$  with  $K_{ij} = \kappa(x_i, x_j)$ . In this work we use the squared exponential kernel:

$$\kappa_{SE}(x, x') = \sigma^2 \exp\left(-\frac{x - x'}{l}\right) \quad 35$$

Where  $\sigma$  and  $l$  determine the vertical variation and the horizontal length scale. The Matérn kernel:

$$\kappa_{MA5}(x, x') = \sigma^2 \left(1 + \frac{\sqrt{5}(x - x')}{\rho} + \frac{5(x - x')^2}{3\rho^2}\right) \exp\left(-\frac{\sqrt{5}(x - x')}{\rho}\right) \quad 36$$

similarly contains the  $\sigma$  parameter controlling vertical variation and  $\rho$  that controls the length scale. The constant kernel prescribes a constant bias in the data independent of  $x$ :

$$\kappa_{CO}(x, x') = \sigma^2 \quad 37$$

The choice of kernel is not trivial and has significant impact on the GP's ability to extrapolate outside of the training range [32]. Fortunately, GP kernels are additive, this means preferential properties from several kernels can be simply combined. For instance, where one kernel predicts short-term variance, and the second kernel predicts a long-term trend. Richardson et al. [17] have shown that combinations of different Matérn and squared exponential kernels possess suitable properties for the prediction of capacity vs. cycle data. They propose usage of correlated capacity-fade data from cells used in a similar manner to construct multi-output GPs. We adopt their approach to parameter-estimate vs. cycle data and use the duplicate cell's parameter estimates (instead of capacity data) to construct the multi-output GP. GPR optimizes the kernels' hyperparameters  $\theta$  by maximizing the log-likelihood function for given observations  $Y$  at the coordinates  $X$ :

$$\log p(Y|X, \theta) \quad 38$$

This problem is not generally convex but random re-initialization of the optimizer is expected to nevertheless find a global optimum. In this work, we use Latin-hypercube sampling [33] to construct a set of 100 initial guess samples from variance and length scale hyperparameters. We then maximize the likelihood for each initial guess and take the best result as the global optimum.

We apply the approach that Richardson et al. [17] proposed for capacity-time series, treating the parameter estimates of target and duplicate cells as multiple outputs. The parameter estimates contain several distinct features that we attempt to model with different kernels. The long-term changes appear relatively slow and smooth, whereas some estimates contain quite significant short-term variance. This makes a summed squared exponential (SE) and matern52 (Ma5) kernel a robust choice [32]. Additionally, we add a constant kernel (CO) to account for a non-zero baseline. The total kernel is results in:

$$\kappa = \kappa_{SE} + \kappa_{Ma5} + \kappa_{CO} \quad 39$$

For more thorough descriptions of kernel design we suggest Ref. [32].

## 4. Experimental

Commercial 2.6 Ah cylindrical cells were subjected to an accelerated degradation study. Acceleration was introduced by elevated temperature and more intense service utilization. The experimental matrix

**Table 4**

Experiment matrix of cycle aging study.

Name	Description	SOC range	C-rate range	Temperature
FR	Frequency regulation	45–55%	$\leq 1C$	40 °C
PS	Peak shaving	22–78%	$\leq 1C$	40 °C
FRPS	Combined FR + PS	16–84%	$\leq 2C$	40 °C
SOC50_40	Calendar aging	50%	–	40 °C
SOC78_40	Calendar aging	78%	–	40 °C
SOC50_25	Calendar aging	50%	–	25 °C

consists of 12 cells, cycled or calendar-aged using six different strategies. Three dynamic cycling protocols for grid-level energy storage applications were designed [21]. Service cycle one (FR) mimics the fast dynamics from a grid frequency regulation application. Cycle two simulates usage for peak shaving (PS), and cycle three is a combination of FR and PS (FRPS). The remaining cells were calendar aged at 50%

SOC and 25 or 40 °C and at 78% SOC at 40 °C. The experimental matrix is given in Table 4.

In regular intervals, reference performance tests (RPT) are carried out. All RPTs are performed at 25 °C in a temperature chamber. The discharge capacity between 4.2 and 2.75 V was measured at C/20 and at 1C rate. Lastly, optimal experiments were performed sequentially during a slow charge preceded by a constant voltage-hold at the target potential with up to 30 min of rest before each OE. The rest-period length was determined to be sufficient at beginning-of-life (BOL). If the cell voltage drifted less than 1 mV per 100 s, the OE was started earlier. An example current time signal for the OEs sequence during the slow charge is given in Supplementary Fig. S 2.

At end-of-test (EOT), validation tests are performed at 25 °C after which cells are opened in a glovebox and electrode samples for scanning electron microscopy (SEM) are harvested from the middle section of the jellyroll. The samples were cross sectioned using a Broad Ion Beam Mill (Hitachi ArBlade 5000). The cross-sections were then imaged using

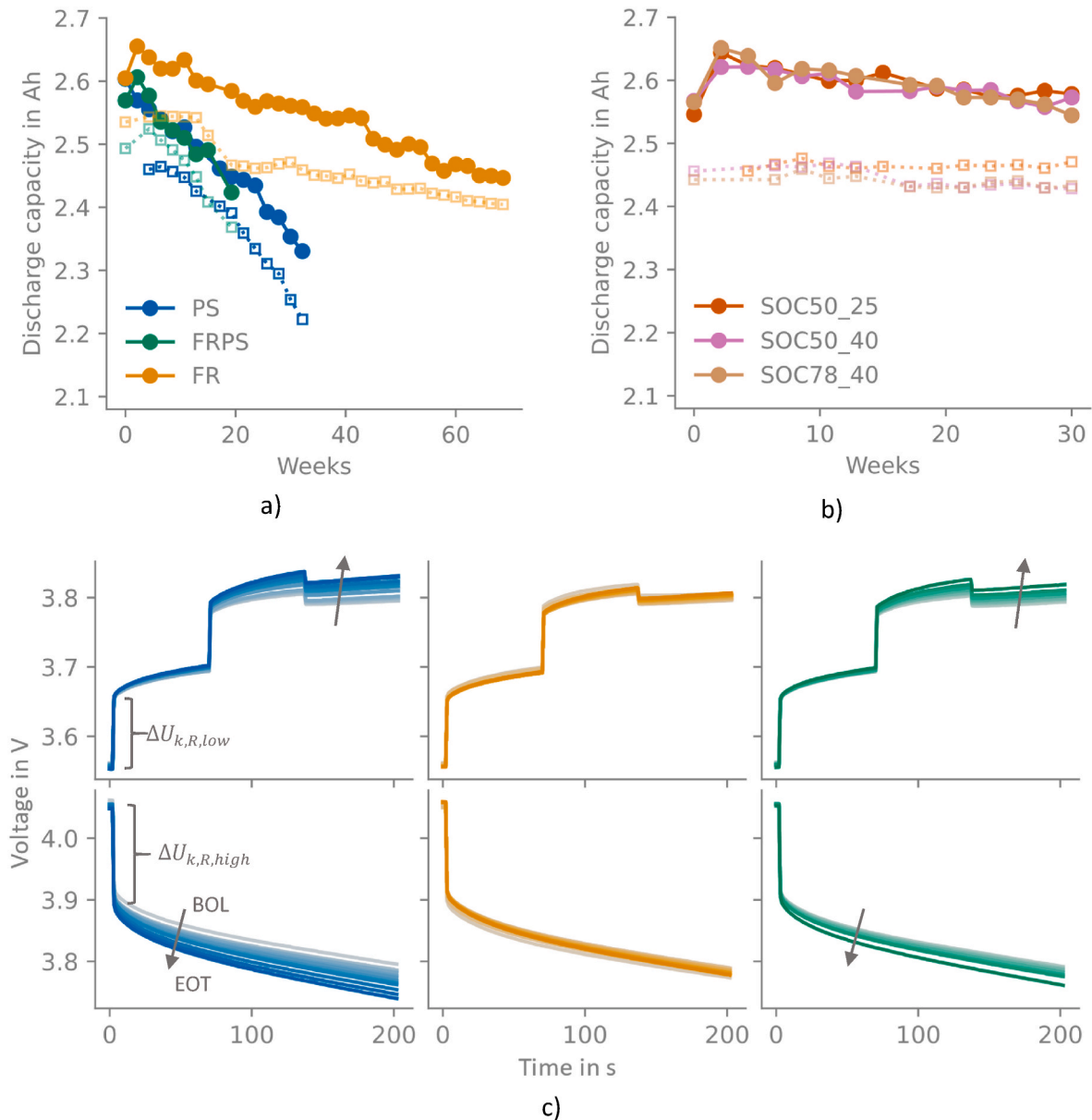


**Fig. 2.** Capacity and dynamic changes of the 12 cells in 6 different groups. Capacity is measured at a C/20 (circle marker) and 1C (square marker) rate. Subfigure a contains C/20 and 1C capacities for cells cycling with different grid-storage service applications. Subfigure b contains C/20 and 1C capacities for cells calendar aged at 50% and 78% SOC as well as at 25 and 40 °C. Subfigure c shows changes in cell voltage response to two optimal current trajectories from BOL (lighter) to EOT (darker) for the PS, FR, and FRPS cells shown in a, remaining experiments are shown in Supplementary Fig. S 3.

secondary electrons using the Zeiss Sigma HD. The SEM micrographs were processed in ImageJ, where they were segmented, cleaned, and quantified. The imaging and subsequent analysis methodology are discussed in detail in Ref. [34].

## 5. Results and discussion

### 5.1. Cycle aging results

The 12 investigated cells were subjected to different cycling and calendar aging regimes. The resulting capacity retention at C/20 and 1C rates is displayed in Fig. 2 a (cycle aged) and b (calendar aged). Calendar aging at elevated temperatures (40 °C) does not lead to significant acceleration in degradation compared to 25°, as measured at 50% SOC. The combined cycle (FRPS) shows the most rapid degradation. In fact, the experiment was stopped after RPT 9 due to a significant resistance increase which caused a violation of specified voltage limits. The frequency regulation service cycle, micro-cycling around 50% SOC, caused more capacity degradation than the comparable calendar aging experiment.

Fig. 2 c shows the three dynamic cells' responses to the optimal current trajectories of OE2 (parameter  $\tau_+$ ) and OE6 (parameter  $\Delta t_+$ ) (compare Supplementary Fig. S 1). Here it is evident that PS and FRPS protocols had distinct impact on the cells compared to FR cycling, where little change in polarization is observed despite similar losses of C/20 capacity at EOT. It is also evident that the ohmic resistance is not the main culprit for this apparent increase in cell resistance, as the ohmic drop between zero and active current at the start of the experiments remains nearly constant. This shows that resistance and capacity alone are not sufficiently descriptive of battery SOH. Cell voltage measurements for the remaining OEs are given in Supplementary Fig. S 3.

### 5.2. Parameter estimates

Dynamic and balancing parameters are re-evaluated at every RPT. Estimates for all 10 model parameters are given in Fig. 3. Parameter trajectories for the three dynamic cycling strategies shown in Fig. 3 a and the three calendar aging protocols in Fig. 3 b confirm a strong dependency of parameter values over cycling time on specific battery usage profiles. Large impact of dynamic cycling, current magnitude, and SOC window can be observed in Fig. 3 a.

Cell balancing is considered through three balancing parameters. The parameters stem from the maximum and minimum state of lithiation in the electrodes, and the balancing represents their individual potential in relation to the total cell voltage. The utilized active volume fraction in both electrodes decreases continuously for all cells, i.e., the amount of stored energy. FRPS-cycling causes the fastest capacity loss. Both the utilization of the negative electrode and the positive electrode decreases at the same rate, the capacity loss therefore mostly stems from loss of lithium.

The PS- and FRPS-cycling show similar trends in most parameter trajectories, indicating a wide SOC window as a main accelerating factor for the degradation. This could already be observed from the capacity measurements in Fig. 2 a. However, access to dynamic model parameters allows dissemination of observed degradation into electrode specific mechanistic contributions at a level that is otherwise only available through cell opening and half-cell testing. For instance, in Fig. 2 c we observe that polarization has increased more in PS cycling than in FRPS cycling, indicating that the PS cell usage allowed more severe degradation without triggering any cut-off voltage conditions. This is confirmed by the tortuosity estimates following a similar trend but the higher equivalent cycle count leads to larger tortuosity at EOT for PS. When comparing to mild cycling conditions (FRPS vs. FR) we observe significant differences in dynamic behavior, despite equivalent C/20 capacity at EOT. The parameter estimates indicate that this is caused by a larger increase in tortuosity in the negative electrode. The tortuosity

and the electrolyte volume fraction are responsible for effective electrolyte transport properties (Eq. 6, 18). A tortuosity increase in the negative electrode could be explained by a decrease in electrolyte volume fraction due to SEI layer growth and indicates worsening of effective electrolyte diffusivity and conductivity. This is observed for PS- and FRPS-cycling. The SEI layer growth is strongly coupled to loss of cyclable lithium (LLI), as lithium gets consumed to form SEI [35]. A high rate of LLI was also seen for PS- and FRPS-cycling, from the evolution of the balancing parameters. The identified decrease in tortuosity in the positive electrode indicates simpler ionic pathways through the electrolyte, this could be caused by swelling of the electrode layers and pore expansion. This is observed in the PS- and FR-cycling, whereas for FRPS  $\tau_+$  seems to stay constant. This indicates a larger swelling in those positive electrodes than in the calendar aged cells.

The overpotential  $\Delta U_{k,R}$  observed when the current is switched on after 5 s in Fig. 2 c contains both the charge-transfer kinetics  $k_{\pm}$  and the ohmic resistance  $R_{cc}$ . At higher cell voltage (Fig. 2 c, row 2), a significant increase can be observed in  $\Delta U_{k,R,high}$  for the PS cell, whereas at lower voltages (Fig. 2 c, row 1)  $\Delta U_{k,R,low}$  is nearly constant. This concentration dependence cannot stem from  $R_{cc}$  and indicates that reaction kinetics are changing. For FRPS this effect persists but for FR kinetics appear to be barely affected. This analysis is confirmed by the parameter estimates in Fig. 3. Kinetic parameters  $k_{\pm}$  are strongly coupled with the electrode specific surface area (Eq. 7 and 21), implying that a decrease in rate constant could in-fact be caused by a decrease in surface area. A surface layer resistance distributed throughout the porous electrode, such as a thickening SEI-layer (Eq. 22), has a similar effect on the cell voltage. Jow et al. [36] note that at elevated temperatures, it is in fact the SEI that is limiting the charge-transfer process in the negative electrode. A decrease in rate-constant is observed in the negative electrode for the harsher FRPS- and PS-cycling. This points at more severe SEI growth opposed to FR-cycling and calendar aging, where  $k_-$  is changing significantly less. PS-cycling also shows a slight increase in rate-constant in the positive electrode (faster kinetics). This likely stems from an increase in surface area.

Diffusion time-constants similarly show significant changes based on usage. While the accuracy is lower than in other parameters, trends can still be observed. In the negative electrode, the diffusion time constant increases distinctly for FR and PS cycles. In the combined cycling (FRPS) and the calendar aging experiments, a decreasing trend is instead observed. An increased diffusion time constant can stem from an increase in diffusion length. The parameter might also include other time constants such as diffusion limited transport through the SEI in the negative electrode [37] or a limiting rock-salt phase at the positive electrode surface [38,39].

Both in PS and FRPS, the positive diffusion time constant  $\Delta t_+$  seems to become sensitive during cycling. Up until that point, it is estimated on the lower bound, which indicates that it is too fast to be identifiable. This shows that an unidentifiable parameter at BOL can become identifiable either by its own impact increasing, or by other parameters becoming less sensitive. In the case of increasing impact for diffusion, this could happen through a shift in cell-balancing and usage of the electrode in a window containing large OCP slopes which are a known pre-requisite for diffusion time constant identifiability [40]. An in-depth identifiability analysis for dynamic model parameters is presented in the validation section.

### 5.3. Validation

#### 5.3.1. Cross validation

We performed a validation of the parameter estimation procedure using optimally designed experiments in previous work [20] including thorough cross validation on full- and half-cell level. In this work, we perform the same full-cell cross validation at end-of-test, this is given in Fig. 4. Here we first show that beginning of life parameters yield

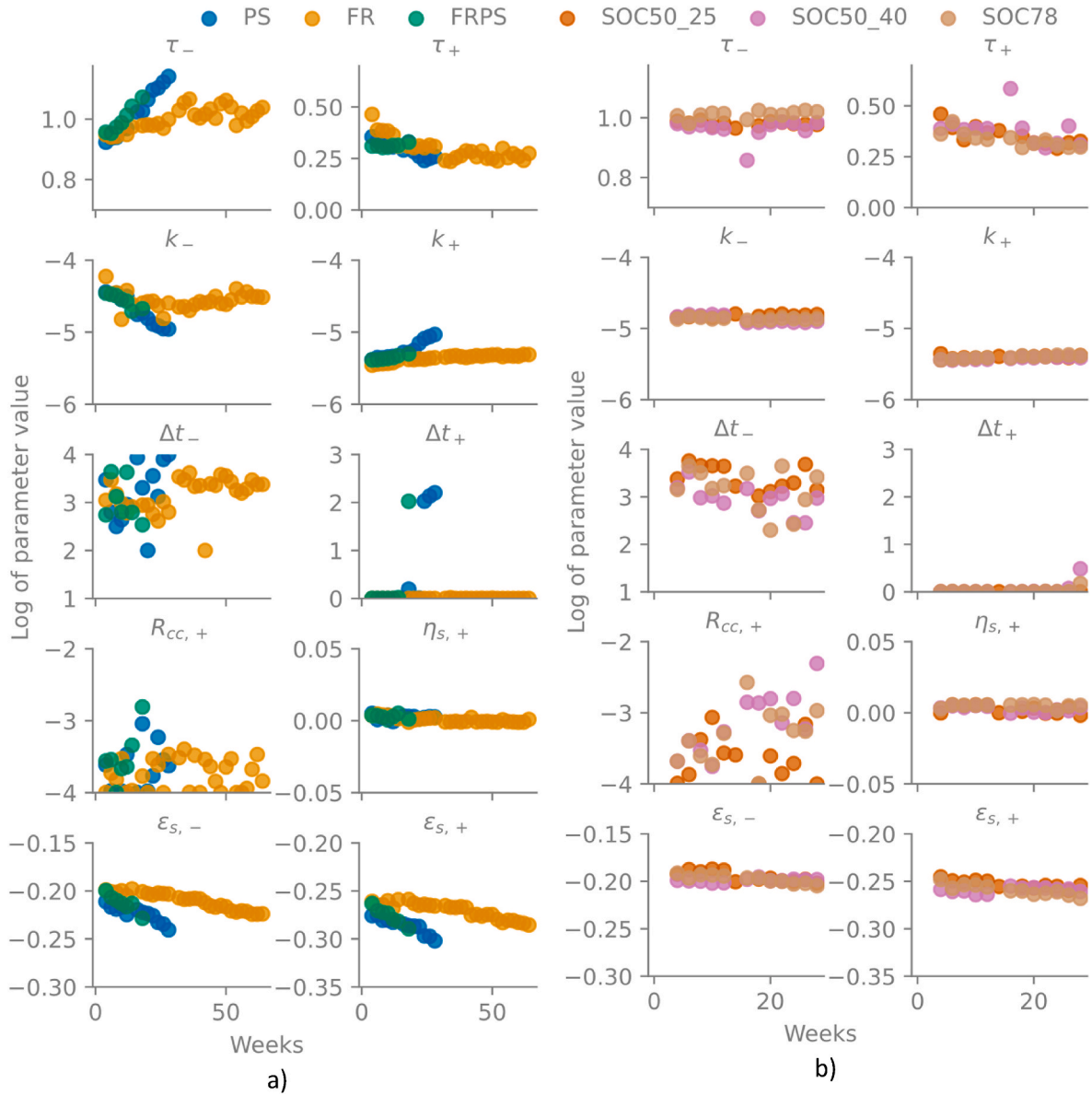


**Fig. 3.**  $\text{Log}_{10}$  of parameter estimates of for the dynamically cycled cells (a) and the calendar aged cells (b). Cell usage significantly changes the parameter trajectories. Significant changes in tortuosity are observed for the PS and FRPS cycles. Circles indicate parameter estimates. A comparison of parameter estimates between duplicate cells is given in [Supplementary Fig. S 6](#) and [Fig. S 8](#).

unsatisfactory model performance at EOT. This is shown by the dotted line representing residuals between model prediction and measurement. The end-of-test parameter estimation significantly improves performance. The RMSE of BOL model prediction could be more than halved for both PS (74–32 mV) and FRPS (62–29 mV) cells by reparametrizing on the optimally designed checkup experiments. The FR cycling RMSE is very low, but the EOT model still outperforms the BOL parametrization. The errors are summarized in [Fig. 4 d](#). Furthermore, we investigated the separate impact of dynamic and balancing parameter evolution on the model prediction and found that updating dynamic model parameters is of equally large importance as updating cell-balancing parameters. We highlight this by including EOT balancing parameters but not EOT dynamic parameters and evaluating the RMSE. We conclude that for wide SOC use-cases it is essential to update both dynamic and balancing parameters to preserve model accuracy whereas model accuracy was acceptable for the FR case without updating any parameters. Some effects are not accurately reproduced even with updated parameters. This can stem both from parameter uncertainty and from model

shortcomings. The systematic error in OE1 likely influences the accuracy of the  $\Delta t_-$  parameter. Fitting errors are increasing slightly for the OE1 experiment but are otherwise relatively constant. They are summarized in [Supplementary Fig. S 4](#). Moreover, some mechanisms cannot be modeled by changes in targeted dynamic model parameters. The relaxation behavior after the constant current segments in [Fig. 4 a](#) is for instance known to be influenced by particle size distributions [41]. This error could therefore be explained by the utilized model's limitations. Already during method development [20], we suggested that SOL dependencies in diffusion coefficients could be necessary for accurate model predictions at extreme SOCs. Finally, the model itself is only an approximation of the real system, this includes for instance the treatment of the real-world 3D geometry as a single 1D slice.

### 5.3.2. Parameter identifiability

As part of the validation, we show that identified parameter estimates are locally sensitive and the sensitivity vectors are linearly independent. We base this identifiability analysis on the procedures



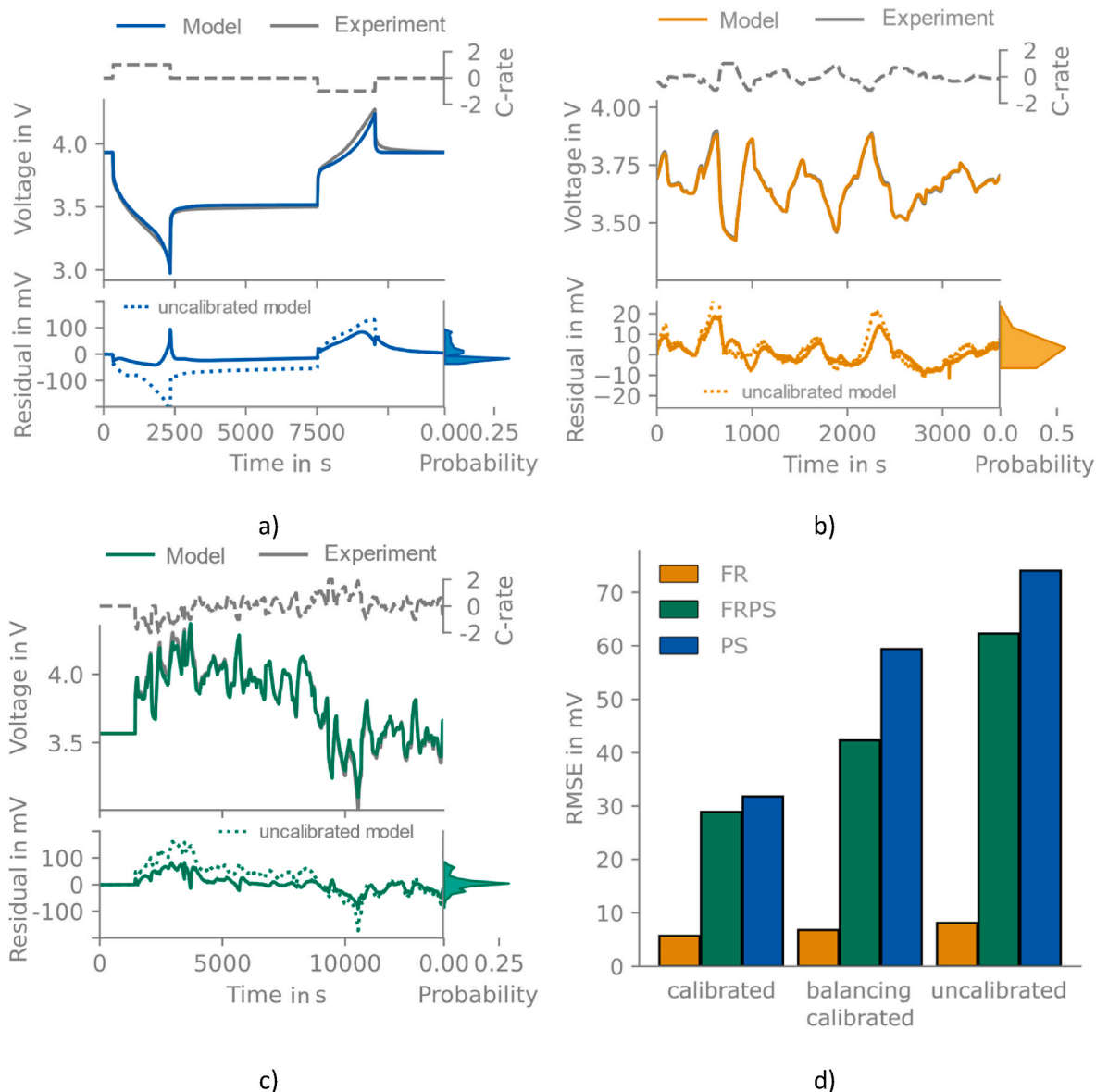


**Fig. 4.** Cross validation of estimated parameter sets at end of test for PS (a), FR (b) and FRPS (c) and associated RMSE values (d). The residuals of the uncalibrated model parameter-sets estimated at beginning of life are shown as dotted lines. For the PS cycle, recalibration of the model lowers the RMSE from 74 mV to 32 mV. For the FRPS experiment, the RMSE is lowered from 63 to 29 mV. For the mildest cycling, the RMSE is reduced from 8 mV to 6 mV. We tested a model with updated balancing parameters and observed improved performance compared to no calibration. However, the dynamic parameters are responsible for most of the observed errors.

described in Ref. [9]. First, we performed a local perturbation of each parameter for each of the optimal experiments to evaluate the sensitivity matrix. If two parameters impact the voltage in the same way, they are linearly dependent, and the rank of the sensitivity matrix would decrease. Second, average local sensitivities are evaluated and ranked. We thus verify that parameters are sensitive and their impact unique, which are the two necessary conditions for practical identifiability [9].

The sensitivity matrices were full rank in all investigated cases. This full sensitivity matrix rank confirmed that all dynamic parameters are identifiable from the optimally designed experiments. We followed the procedure detailed in Ref. [42].

The numerical gradient is evaluated by taking 0.5% of the parameter range Table 3 and comparing the perturbed cell voltage with the simulation at the nominal parameter estimate. The average residuals for the parameters at EOT for each cycling regime are given in Fig. 5. Fig. 5 a shows identifiability in the three dynamic cycling protocols and b shows parameter identifiability of calendar aged cells. Residual time-series for

the FRPS cell at EOL are given in Supplementary Fig. S 7.

All parameters show sensitivity; however, the magnitudes vary significantly. The largest residuals are observed for kinetic rate constants that are impactful in all 8 optimal experiments, followed by tortuosities, diffusion time constants, and finally the least sensitive parameter being the current collector contact resistance. This is in accordance with the identified parameter trajectories in Fig. 3, where the trajectories show a larger variance for diffusion time constants and the resistance parameter.

### 5.3.3. Microscopy and image analysis

Cross-section imaging was performed after EOT for FRPS and PS samples as well as at BOL for a reference cell. The image of the double-sided coated electrode, of the FRPS cell at EOT and the BOL reference are given in Fig. 6. A qualitative comparison of the positive electrode in Fig. 6 a and b does not allow certain conclusions. The negative electrode in Fig. 6 c and d appears less porous at EOT. This aligns with the

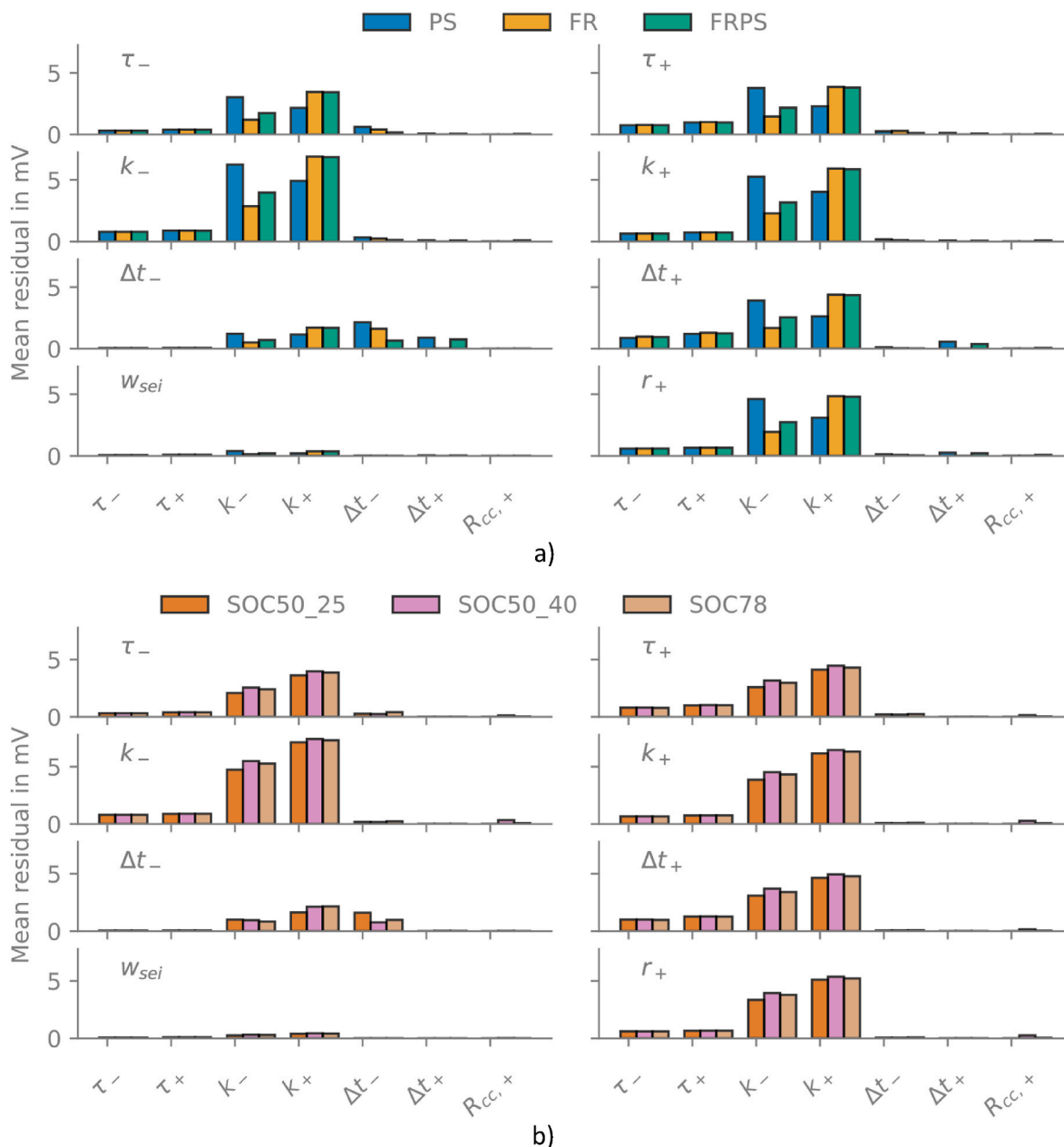


**Fig. 5.** Posterior parameter identifiability for the last checkup of the dynamic cycles (a) and the calendar aging cycles (b). Bar size indicates identifiable parameters. Each of the 8 designed experiments is simulated both with the identified parameter set, and then with a perturbed step for one parameter at a time. The perturbation is chosen as 0.5% of the investigated range. Each bar then shows the impact individual perturbations have in a specific optimal experiment by taking the mean of the magnitude of the difference between perturbed and un-perturbed simulation of the cell voltage. For instance, in the experiment designed for the negative electrode diffusion time constant  $\Delta t_-$ , the target parameter is the most important one, as it has the highest impact on the cell voltage. Both rate-constants are impactful throughout all experiments, indicating a robust identification. Tortuosity is important in the associated experiments but also in the experiment designed for  $\Delta t_+$ . The parameter with the smallest impact at the identified value is the lumped current collector contact resistance. For the calendar aging experiments, identifiability is nearly equivalent between the different aging regimes.

observed increase in tortuosity in the FRPS and PS cycling. We also observed a copper deposit near the separator interface. EDX imaging of the region is given in the supplementary material. As the copper was likely dissolved from the negative current collector and then redeposited, it is likely that this would manifest in a resistance increase, which correlates with the observed increase in current collector increase in the PS and FRPS cycling in Fig. 3. Graphite delamination was observed in the PS negative electrode at EOT (see Fig. 6 e and Supplementary Fig. S 5). This has been observed before and the crack propagation assigned to either solvent co-intercalation or the stress due to lithium intercalation [43,44].

In a subsequent image analysis of the cross sections, equivalent particle diameters and electrode thickness were determined. This is shown in Fig. 6 f and g. The PS cycling shows a significantly reduced mean particle size (more than 0.5  $\mu\text{m}$ ), this implies that more secondary particles have broken up into primary particles. This would lead to a significant increase in surface area and appear as an increase of the positive electrode rate-constant in our parameterization. We observe a significantly larger increase in rate-constant in PS than in FRPS in Fig. 3, which supports the connection between particle size, surface area, and kinetic rate-constants in the positive electrode. This was not the case for FRPS cycling or the calendar aged cells at 78% SOC.

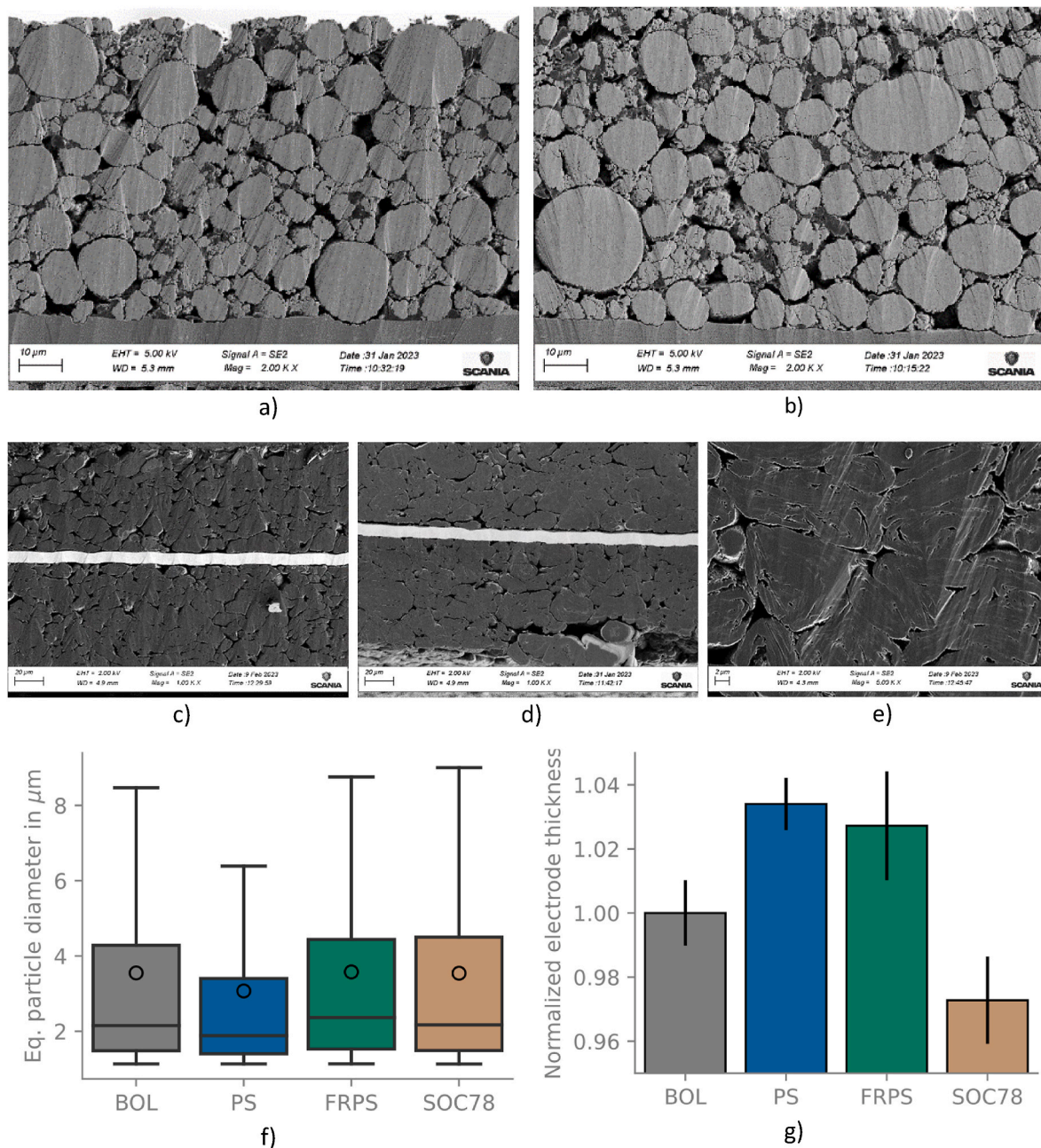


**Fig. 6.** SEM cross-sections at BOL (a, c) and EOT (b, d, e) for the positive electrode (a, b) and the negative electrode (c, d). Changes in the positive electrode are barely observable. However, in the negative electrode, some copper deposit is observed on a graphite particle near the separator at EOT. Additionally, the negative electrode shows an increase in micro-cracks. This is in accordance with behavior observed by Lin et al. [43]. A close-up cross-section of the PS post-mortem samples showing graphite delamination is given in e. Subfigure f shows the boxplot of equivalent positive particle diameters (with the mean denoted by a circle) and g reveals thicknesses changes of the double-sided positive electrode. Compared to BOL, the FRPS cycle has a similar equivalent diameter, whereas the PS cycle shows a significant decrease of the mean particle size by more than 0.5  $\mu\text{m}$ . The electrode thickness increases by 2.5–3% during cycling, whereas it decreases by a similar magnitude during calendar aging at high SOC.

We found that both FRPS and PS cycling lead to significant layer expansion of  $\sim 3\%$  (4–5  $\mu\text{m}$ ) of the BOL thickness. Additional to the active material, the electrode matrix consists of a carbon additive and a binder phase for electrical conductivity and mechanical integrity. The binder is known to alleviate stresses generated in the particles [45] and electrode swelling has been observed at EOT. This could be caused by a plastic deformation and expansion of the binder phase caused for instance by particles cracking and applying forces on the binder phase. The increase in thickness might be responsible for the decrease in positive electrode tortuosity observed in Fig. 3 for the PS cell. However, a

nearly constant tortuosity estimate was observed for the FRPS cell which does not correlate with the measured thickness increase. The PS experiment applied constant currents which causes more lithium concentration polarization dependent stresses [46] in the particles than the more dynamic FRPS experiment. This could result in more cracking which would explain the observed decrease in tortuosity in PS vs FRPS experiments. The thickness measure does not capture z-direction variation of thickness which might be significant.

#### 5.4. Trajectory extrapolation

It is evident from the parameter estimates shown in Fig. 3 that nearly all parameters follow a certain trend. In this section we demonstrate extrapolation of parameter trajectories using multi-output GPR.

As the calendar aging experiments caused very little degradation, we focus here on the two dynamic cycling strategies FR, and FRPS. For PS, the duplicate cell contained systematic measurement error from a malfunctioning potentiostat channel and could therefore not be included in the training set. A single output GPR for the faultless PS cell is shown in Supplementary Fig. S 8. Richardson et al. [17] showed that multi-output GPR approaches greatly improved GPR predictive capability which our result confirms. We therefore focus our analysis on the FR and FRPS cells where complete duplicate measurements were available.

Resulting predictions for FR and FRPS are given in Fig. 7. For the FR cycle in Fig. 7 a, 12 RPTs of both FRa and FRb duplicate cells are used to train the GP. Further 20 RPTs of FRa are shown as empty markers as validation of prediction accuracy. All estimates in the validation set lie within the shaded 95% confidence region of the prediction. The posterior mean, highlighted by a line, is an accurate prediction of cell parameter changes looking ahead more than 1000 cycles. High uncertainty of the posterior e.g., for prediction of  $\tau_+$  and  $\Delta t_-$  is a result of the larger uncertainty in those parameter estimates, which in turn implies their low importance to cell voltage. This will therefore have only a small impact on the model uncertainty.

We use the estimated parameter likelihoods to evaluate 1C discharge experiments. The mean parameter predictions are used to evaluate mean capacity predictions. Then, samples of the estimated parameter

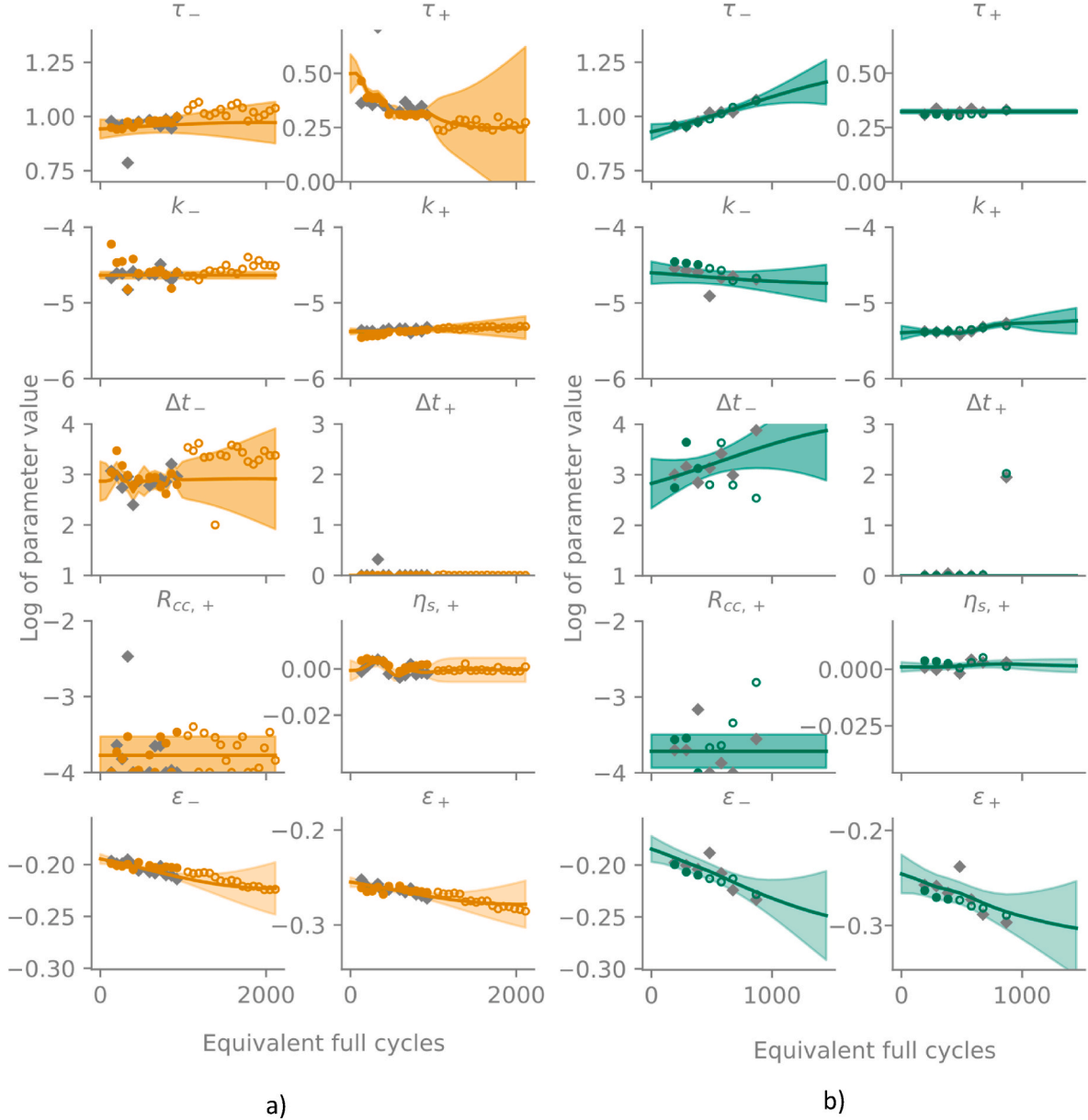


**Fig. 7.** Parameter trajectory extrapolation using a multi-output gaussian process for FR (a) and FRPS (b). For FR in (a) the first 12 RPT of both duplicate cells are part of the training set, this is indicated by filled markers. The posterior mean is highlighted by a line and 95% confidence intervals are shown as a shaded area. The validation set, shown by empty markers, generally lies within this 95% confidence interval and the posterior mean value is a very good prediction of the parameter estimate. For the FRPS cell, where only 9 RPTs were available, all 9 samples of the duplicate cell and 3 samples of the target cell are included in the training set. The 6 remaining samples are again used for cross validation. All validation samples lie within the confidence interval and the posterior mean of the GPR offers a very good prediction of the cell parameters. In case a, the proposed model accurately predicts cell parameters up to 1000 cycles forward when much data is available. In case b, only 3 data-points of the target cell are required for an accurate prediction of up to 500 cycles in the future.



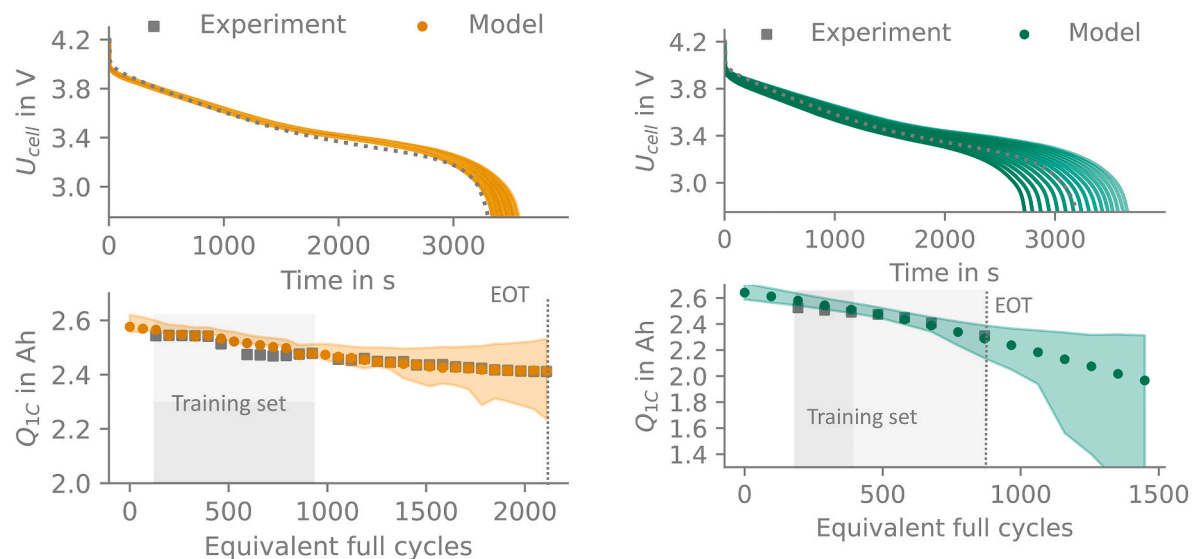


**Fig. 8.** 1C discharge prediction and experimental validation for FR (a) and FRPS (b) cells. The EOT 1C discharge is included as a gray dotted line in the upper subplots. The lower subplots contain measured, and model estimated 1C discharge capacities as well as 95% confidence intervals of the prediction. It is evident that the model accurately matches the real cell at every stage of testing. Furthermore, parameter trends can be interpolated to make a capacity prediction for any given use-case at every state-of-health. Parameter trajectories can also be extrapolated beyond the training data as shown in Fig. 7. In a, we show that when using this extrapolation, the model accurately predicts 1C discharge capacity at 2100 cycles when using only sub 900 cycle training data. In b, all duplicate cell checkups but only the 3 first data-points for the target cell are used for training.

uncertainty space are drawn using Latin-hypercube sampling. Each sample corresponds to a parameter vector and is used to simulate a 1C discharge, giving a distribution of 1C discharge capacities at each step. The mean capacity predictions and the distributions' 95% confidence interval are shown in Fig. 8.

For the FR cells in Fig. 8 a, the GP is trained on 12 RPTs for FRa and FRb. The prediction is validated against the 1C discharge measurements more than 1000 cycles ahead of training data and predicts the measured 1C discharge capacity with <1% error. For the FRPS cells, only 7 RPTs were available until EOT when polarization-increase caused the service cycle to break voltage limits. In this case, the full duplicate cell, and 3 samples of the target cell are used for training, and 4 final samples of the target cell are used for validation. The 1C capacity prediction is extremely accurate at EOT with <1% prediction error. A comparison with a simpler linear model for parameter extrapolation and subsequent discharge capacity prediction is given in Supplementary Fig. S 9. Both the accuracy of the parameter extrapolation and the capacity prediction is significantly worse. Additionally, we include a linear extrapolation based on the capacity measurements of the first 12 RPTs, which shows an overestimation of the capacity loss.

Using the available data-set, only a limited validation of the approaches capability was possible as too few data-points were available for more heavily degrading cells and the most complete data-set showed more linear degradation. We nevertheless believe the proposed approach is relevant for applications where data at various SOH is available to reinforce the GP. Both to diagnose the batteries present SOH, but also for prognosis of future degradation, rate-capability, and capacity fade.

## 6. Summary and conclusion

In this paper, we show the evolution of electrochemical model parameters throughout cycle life for three dynamic and three calendar aging protocols. Parameter estimation was performed on optimally designed checkout experiments that maximize sensitivity based on previous published work [20]. A balancing model is calibrated at each checkout using a C/20 constant current discharge experiment. We first summarized the obtained parameter estimates, discussed observed parameter changes, and suggested responsible aging mechanisms. We then proposed a

parameter extrapolation scheme based on Gaussian Process Regression (GPR) to extrapolate from observed estimates and tested this approach on the three dynamic cycling protocols PS, FR and FRPS. We showed that GPR outperforms a linear extrapolation both in parameter and predicted model accuracy. We demonstrated the extrapolated model's accuracy by comparing its predictions with measured 1C discharge capacities. To validate the parameter estimates, we first showed that the BOL parametrization is less accurate in all investigated cases. Furthermore, we demonstrated that both dynamic and balancing parameters are required to accurately predict dynamic model behavior.

Next, we studied identifiability of the presented parameter estimates by evaluating the local derivative of the model output with respect to the parameter estimate. We could show that all investigated parameters are sensitive, and the optimally designed experiments predicted conditions in which parameters are sensitive accurately. Additionally, we confirmed that the local derivatives of parameter estimates are linearly independent and therefore fulfill the second identifiability requirement of parameter impact being unique [9]. Finally, we performed a cell opening and compared BIB-SEM cross-sections of the aged materials with BOL samples. Quantitative comparison by means of image analysis showed that dynamic cycling caused significant increase in layer thickness and particle size distribution in the positive electrode. In the negative electrode an increased delamination of the graphite could be observed.

We then proposed a parameter extrapolation scheme based on GPR to extrapolate from observed estimates and tested this approach on the three dynamic cycling protocols PS, FR and FRPS. We showed that GPR outperforms linear extrapolation both in parameter and predicted model accuracy. We demonstrated the extrapolated model's accuracy by comparing its predictions with measured 1C discharge capacities. To validate the parameter estimates, we first showed that the BOL parametrization is less accurate in all investigated cases. Furthermore, we demonstrated that both dynamic and balancing parameters are required to accurately predict dynamic model behavior. With this summary, our key conclusions are.

- Model parameters change significantly and both dynamic and balancing parameters must be updated to preserve model accuracy. We show that updating balancing parameters alone comes with a significant penalty in model accuracy of 15–50% increased root-

mean-square error (RMSE) whereas not updating any parameters at all comes with a 30–65% penalty in RMSE.

- A thorough validation study confirms parameter identifiability by showing they are locally sensitive and their impact linearly independent. We also show how identifiability depends on cycle-life. Insensitive parameters at BOL could become sensitive. This is observed for the positive electrode diffusion time constant which becomes sensitive both for the PS and FRPS cells after 5–8% capacity loss.
- Changes in electrochemical model parameters correlate with observed micro-structural changes and are therefore useful indicators of state-of-health. We observed an increase in positive electrode layer thicknesses using BIB-SEM image analysis which explains the decrease in tortuosity observed through re-parametrization. The tortuosity increase in the negative electrode can be explained by the observed delamination and the SEI layer growth.
- Parameter extrapolation using GPR accurately predicts model parameters both in short- and long-term prediction. For the FR cells, the 1C discharge capacity after 2200 cycles could be accurately predicted using only <900 cycle training data. Furthermore, the uncertainty of the parameter prediction can be used to estimate uncertainty for any sort of prediction. In this case, the 2200 cycle capacity is predicted with a 5% SOH confidence interval.

The combination of the physics-based model with a machine-learning based extrapolation approach allows prediction of future model behavior in any conceivable use case. Furthermore, we note that the approach using optimally designed experiments ensured that parameters were identifiable by both maximizing sensitivity and minimizing interdependency.

#### CRedit authorship contribution statement

**Moritz Streb:** Conceptualization, Methodology, Software, Validation, Formal analysis, Investigation, Writing – original draft, Writing – review & editing, Visualization. **Mathilda Ohrelius:** Methodology, Validation, Investigation, Writing – original draft, Visualization. **Aamer Siddiqui:** Formal analysis, Investigation. **Matilda Klett:** Writing – review & editing, Supervision, Funding acquisition. **Göran Lindbergh:** Writing – review & editing, Supervision, Funding acquisition.

#### Declaration of competing interest

The authors declare that they have no known competing financial interests or personal relationships that could have appeared to influence the work reported in this paper.

#### Data availability

Data will be made available on request.

#### Acknowledgement

This work was funded by the Swedish Energy Agency through the FFI program Energy and Environment (project number 47103–1), the Swedish Electromobility Center and SweGRIDS (project number FPS16). It was conducted within the framework Batteries Sweden BASE. M.S. thanks Malin Andersson for thoughtful discussions on the manuscript.

#### Appendix A. Supplementary data

Supplementary data to this article can be found online at <https://doi.org/10.1016/j.jpowsour.2023.233686>.

#### Acronyms

Acronyms are listed in Table 5.

**Table 5**  
List of acronyms.

Acronym	Meaning
BOL	Beginning-of-life
EOT	End-of-test
NMC532	$\text{LiNi}_{0.5}\text{Mn}_{0.3}\text{Co}_{0.2}\text{O}_2$
RMSE	Root-mean-square error
GP	Gaussian process
GPR	Gaussian process regression
FR	Frequency regulation
PS	Peak shaving
FRPS	Frequency regulation and peak shaving
LLI	Loss of lithium
RPT	Reference performance test
EIS	Electrochemical impedance spectroscopy
BMS	Battery management system
SOH	State-of-health
OE	Optimal experiment
SEI	Solid electrolyte interphase
DFN	Doyle-Fuller-Newman
SOC	State-of-charge
SOL	State-of-lithiation
OCV	Open-circuit potential
BIB-SEM	Broad ion beam scanning electron microscopy

#### References

- [1] A. Masias, J. Marcicki, W.A. Paxton, Opportunities and challenges of lithium ion batteries in automotive applications, *ACS Energy Lett.* 6 (2021) 621–630, <https://doi.org/10.1021/acsenergylett.0c02584>.
- [2] A. Tomaszewska, Z. Chu, X. Feng, S. O'Kane, X. Liu, J. Chen, C. Ji, E. Endler, R. Li, L. Liu, Y. Li, S. Zheng, S. Vetterlein, M. Gao, J. Du, M. Parkes, M. Ouyang, M. Marinescu, G. Offer, B. Wu, Lithium-ion battery fast charging: a review, *ETransportation* 1 (2019), 100011, <https://doi.org/10.1016/j.etrans.2019.100011>.
- [3] X. Han, L. Lu, Y. Zheng, X. Feng, Z. Li, J. Li, M. Ouyang, A review on the key issues of the lithium ion battery degradation among the whole life cycle, *ETransportation* 1 (2019), 100005, <https://doi.org/10.1016/j.etrans.2019.100005>.
- [4] C. Helbig, A.M. Bradshaw, L. Wietschel, A. Thorenz, A. Tuma, Supply risks associated with lithium-ion battery materials, *J. Clean. Prod.* 172 (2018) 274–286, <https://doi.org/10.1016/j.jclepro.2017.10.122>.
- [5] G. Harper, R. Sommerville, E. Kendrick, L. Driscoll, P. Slater, R. Stolkin, A. Walton, P. Christensen, O. Heidrich, S. Lambert, A. Abbott, K. Ryder, L. Gaines, P. Anderson, Recycling lithium-ion batteries from electric vehicles, *Nature* 575 (2019) 75–86, <https://doi.org/10.1038/s41586-019-1682-5>.
- [6] E. Martinez-Laserna, I. Gandiaga, E. Sarasketa-Zabala, J. Badedo, D.-I. Stroe, M. Swierczynski, A. Goikoetxea, Battery second life: hype, hope or reality? A critical review of the state of the art, *Renew. Sustain. Energy Rev.* 93 (2018) 701–718, <https://doi.org/10.1016/j.rser.2018.04.035>.
- [7] G. Zubi, R. Dufo-López, M. Carvalho, G. Pasaoglu, The lithium-ion battery: state of the art and future perspectives, *Renew. Sustain. Energy Rev.* 89 (2018) 292–308, <https://doi.org/10.1016/j.rser.2018.03.002>.
- [8] M. Streb, M. Andersson, V. Löfqvist Klass, M. Klett, M. Johansson, G. Lindbergh, Investigating re-parametrization of electrochemical model-based battery management using real-world driving data, *ETransportation* 16 (2023), 100231, <https://doi.org/10.1016/j.etrans.2023.100231>.
- [9] M. Andersson, M. Streb, J.Y. Ko, V. Löfqvist Klass, M. Klett, H. Ekström, M. Johansson, G. Lindbergh, Parametrization of physics-based battery models from input–output data: a review of methodology and current research, *J. Power Sources* 521 (2022), 230859, <https://doi.org/10.1016/j.jpowsour.2021.230859>.
- [10] Y. Li, D.M. Vilathgamuwa, E. Wikner, Z. Wei, X. Zhang, T. Thiringer, T. Wik, C. Zou, Electrochemical model-based fast charging: physical constraint-triggered PI control, *IEEE Trans. Energy Convers.* 36 (2021) 3208–3220, <https://doi.org/10.1109/TEC.2021.3065983>.
- [11] Y. Bi, Y. Yin, S.-Y. Choe, Online state of health and aging parameter estimation using a physics-based life model with a particle filter, *J. Power Sources* 476 (2020), 228655, <https://doi.org/10.1016/j.jpowsour.2020.228655>.
- [12] V. Sulzer, P. Mohtat, A. Aitio, S. Lee, Y.T. Yeh, F. Steinbacher, M.U. Khan, J.W. Lee, J.B. Siegel, A.G. Stefanopoulou, D.A. Howey, The challenge and opportunity of battery lifetime prediction from field data, *Joule* 5 (2021) 1934–1955, <https://doi.org/10.1016/j.joule.2021.06.005>.
- [13] M. Doyle, T. Fuller, J. Newman, Modelling of the galvanostatic charge and discharge of the lithium/polymer/insertion cell, *J. Electrochem. Soc.* 140 (1993) 1526–1533, <https://doi.org/10.1149/1.2221597>.

- [14] K.S. Mayilvahanan, J.R. Soni, K.J. Takeuchi, E.S. Takeuchi, A.C. Marschilok, A. C. West, Parameter estimation for electrode degradation: learning in the face of model-experiment discrepancies, *J. Electrochem. Soc.* 169 (2022), 050517, <https://doi.org/10.1149/1945-7111/ac6c0e>.
- [15] K.S. Mayilvahanan, A. Nicoll, J.R. Soni, K.J. Takeuchi, E.S. Takeuchi, A. C. Marschilok, A.C. West, Physics-based models, machine learning, and experiment: towards understanding complex electrode degradation, *J. Electrochem. Soc.* 170 (2023), 010502, <https://doi.org/10.1149/1945-7111/acadab>.
- [16] C. Lyu, Y. Song, J. Zheng, W. Luo, G. Hinds, J. Li, L. Wang, In situ monitoring of lithium-ion battery degradation using an electrochemical model, *Appl. Energy* 250 (2019) 685–696, <https://doi.org/10.1016/j.apenergy.2019.05.038>.
- [17] R.R. Richardson, M.A. Osborne, D.A. Howey, Gaussian process regression for forecasting battery state of health, *J. Power Sources* 357 (2017) 209–219, <https://doi.org/10.1016/j.jpowsour.2017.05.004>.
- [18] D. Yang, X. Zhang, R. Pan, Y. Wang, Z. Chen, A novel Gaussian process regression model for state-of-health estimation of lithium-ion battery using charging curve, *J. Power Sources* 384 (2018) 387–395, <https://doi.org/10.1016/j.jpowsour.2018.03.015>.
- [19] P. Tagade, K.S. Hariharan, S. Ramachandran, A. Khandelwal, A. Naha, S.M. Kolake, S.H. Han, Deep Gaussian process regression for lithium-ion battery health prognosis and degradation mode diagnosis, *J. Power Sources* 445 (2020), 227281, <https://doi.org/10.1016/j.jpowsour.2019.227281>.
- [20] M. Streb, M. Ohrelus, M. Klett, G. Lindbergh, Improving Li-ion battery parameter estimation by global optimal experiment design, *J. Energy Storage* 56 (2022), 105948, <https://doi.org/10.1016/j.est.2022.105948>.
- [21] M. Ohrelus, M. Berg, R. Wreland Lindström, G. Lindbergh, Lifetime limitations in multi-service battery energy storage systems, *Energies* 16 (2023) 3003, <https://doi.org/10.3390/en16073003>.
- [22] U. Krewer, F. Röder, E. Harinath, R.D. Braatz, B. Bedürftig, R. Findeisen, Review—dynamic models of Li-ion batteries for diagnosis and operation: a review and perspective, *J. Electrochem. Soc.* 165 (2018) A3656–A3673, <https://doi.org/10.1149/2.1061814jes>.
- [23] V. Sulzer, S.G. Marquis, R. Timms, M. Robinson, S.J. Chapman, Python battery mathematical modelling (PyBaMM), *J. Open Res. Software* 9 (2021) 14, <https://doi.org/10.5334/jors.309>.
- [24] J.C. Forman, S.J. Moura, J.L. Stein, H.K. Fathy, Genetic identification and Fisher identifiability analysis of the Doyle–Fuller–Newman model from experimental cycling of a LiFePO<sub>4</sub> cell, *J. Power Sources* 210 (2012) 263–275, <https://doi.org/10.1016/j.jpowsour.2012.03.009>.
- [25] P. Mohtat, S. Lee, V. Sulzer, J.B. Siegel, A.G. Stefanopoulou, Differential expansion and voltage model for Li-ion batteries at practical charging rates, *J. Electrochem. Soc.* 167 (2020), 110561, <https://doi.org/10.1149/1945-7111/aba5d1>.
- [26] M. Safari, M. Morcrette, A. Teyssot, C. Delacourt, Multimodal physics-based aging model for life prediction of Li-ion batteries, *J. Electrochem. Soc.* 156 (2009) A145, <https://doi.org/10.1149/1.3043429>.
- [27] J. Landesfeind, H.A. Gasteiger, Temperature and concentration dependence of the ionic transport properties of lithium-ion battery electrolytes, *J. Electrochem. Soc.* 166 (2019) A3079–A3097, <https://doi.org/10.1149/2.0571912jes>.
- [28] S.G. Marquis, V. Sulzer, R. Timms, C.P. Please, S.J. Chapman, An asymptotic derivation of a single particle model with electrolyte, *J. Electrochem. Soc.* 166 (2019) A3693–A3706, <https://doi.org/10.1149/2.0341915jes>.
- [29] C. Cartis, J. Fiala, B. Marteau, L. Roberts, Improving the flexibility and robustness of model-based derivative-free optimization solvers, *ACM Trans. Math Software* 45 (2019) 1–41, <https://doi.org/10.1145/3338517>.
- [30] K.P. Murphy, *Machine Learning: a Probabilistic Perspective*, Cambridge, MA, 2012.
- [31] A.G. de G. Matthews, M. van der Wilk, T. Nickson, Keisuke Fujii, A. Boukouvalas, P. León-Villagrà, Z. Ghahramani, J. Hensman, GPflow: a Gaussian process library using TensorFlow, *J. Mach. Learn. Res.* 18 (2017) 1–6.
- [32] D.K. Duvenaud, *Automatic Model Construction with Gaussian Processes*, University of Cambridge, 2014.
- [33] J.C. Helton, F.J. Davis, J.D. Johnson, A comparison of uncertainty and sensitivity analysis results obtained with random and Latin hypercube sampling, *Reliab. Eng. Syst. Saf.* 89 (2005) 305–330, <https://doi.org/10.1016/j.res.2004.09.006>.
- [34] Saleem Siddiqui, Aamer Mohammed, Broad Ion Beam Cross-Sectioning, Microscopy, and Image Analysis of Battery Electrode Morphology, 2022.
- [35] J. Zhu, M.S. Dewi Darma, M. Knapp, D.R. Sørensen, M. Heere, Q. Fang, X. Wang, H. Dai, L. Mereacre, A. Senyshyn, X. Wei, H. Ehrenberg, Investigation of lithium-ion battery degradation mechanisms by combining differential voltage analysis and alternating current impedance, *J. Power Sources* 448 (2020), 227575, <https://doi.org/10.1016/j.jpowsour.2019.227575>.
- [36] T.R. Jow, S.A. Delp, J.L. Allen, J.-P. Jones, M.C. Smart, Factors limiting Li<sup>+</sup> charge transfer kinetics in Li-ion batteries, *J. Electrochem. Soc.* 165 (2018) A361–A367, <https://doi.org/10.1149/2.1221802jes>.
- [37] C. Yan, R. Xu, Y. Xiao, J. Ding, L. Xu, B. Li, J. Huang, Toward critical electrode/electrolyte interfaces in rechargeable batteries, *Adv. Funct. Mater.* 30 (2020), 1909887, <https://doi.org/10.1002/adfm.201909887>.
- [38] S.-K. Jung, H. Gwon, J. Hong, K.-Y. Park, D.-H. Seo, H. Kim, J. Hyun, W. Yang, K. Kang, Understanding the degradation mechanisms of LiNi<sub>0.5</sub>Co<sub>0.2</sub>Mn<sub>0.3</sub>O<sub>2</sub> cathode material in lithium ion batteries, *Adv. Energy Mater.* 4 (2014), 1300787, <https://doi.org/10.1002/aenm.201300787>.
- [39] J.-Z. Kong, C. Ren, G.-A. Tai, X. Zhang, A.-D. Li, D. Wu, H. Li, F. Zhou, Ultrathin ZnO coating for improved electrochemical performance of LiNi<sub>0.5</sub>Co<sub>0.2</sub>Mn<sub>0.3</sub>O<sub>2</sub> cathode material, *J. Power Sources* 266 (2014) 433–439, <https://doi.org/10.1016/j.jpowsour.2014.05.027>.
- [40] A.M. Bizeray, J. Kim, S.R. Duncan, D.A. Howey, Identifiability and parameter estimation of the single particle lithium-ion battery model, *IEEE Trans. Control Syst. Technol.* 27 (2019) 1862–1877, <https://doi.org/10.1109/TCST.2018.2838097>.
- [41] T.L. Kirk, J. Evans, C.P. Please, S.J. Chapman, Modeling electrode heterogeneity in lithium-ion batteries: unimodal and bimodal particle-size distributions, *SIAM J. Appl. Math.* 82 (2022) 625–653, <https://doi.org/10.1137/20M1344305>.
- [42] D.C. López, C. G. Wozny, A. Flores-Tlacuahuac, R. Vasquez-Medrano, V.M. Zavala, A computational framework for identifiability and ill-conditioning analysis of lithium-ion battery models, *Ind. Eng. Chem. Res.* 55 (2016) 3026–3042, <https://doi.org/10.1021/acs.iecr.5b03910>.
- [43] N. Lin, Z. Jia, Z. Wang, H. Zhao, G. Ai, X. Song, Y. Bai, V. Battaglia, C. Sun, J. Qiao, K. Wu, G. Liu, Understanding the crack formation of graphite particles in cycled commercial lithium-ion batteries by focused ion beam - scanning electron microscopy, *J. Power Sources* 365 (2017) 235–239, <https://doi.org/10.1016/j.jpowsour.2017.08.045>.
- [44] B.W. Sheldon, A. Tokranov, Internal stress due to solvent co-intercalation in graphite electrodes for Li ion batteries, *Extreme Mech. Lett.* 9 (2016) 379–385, <https://doi.org/10.1016/j.eml.2016.05.001>.
- [45] B. Koo, H. Kim, Y. Cho, K.T. Lee, N.-S. Choi, J. Cho, A highly cross-linked polymeric binder for high-performance silicon negative electrodes in lithium ion batteries, *Angew. Chem.* 124 (2012) 8892–8897.
- [46] J.Y. Ko, M. Varini, M. Klett, H. Ekström, G. Lindbergh, Porous electrode model with particle stress effects for Li(Ni<sub>1/3</sub>Co<sub>1/3</sub>Mn<sub>1/3</sub>)O<sub>2</sub> electrode, *J. Electrochem. Soc.* 166 (2019) A2939–A2949, <https://doi.org/10.1149/2.0661913jes>.